

X-Ray Observations of the edge-on star-forming galaxy NGC 891 and its supernova SN1986J

Rowan F. Temple^{*}, Somak Raychaudhury and Ian R. Stevens

School of Physics and Astronomy, University of Birmingham, Edgbaston, Birmingham B15 2TT, England

Accepted yyyy mm dd. Received yyyy mm dd; in original form yyyy mm dd

ABSTRACT

We present *XMM-Newton* observations of NGC 891, a nearby edge-on spiral galaxy. We analyse the extent of the diffuse emission emitted from the disk of the galaxy, and find that it has a single temperature profile with best fitting temperature of 0.26 keV, though the fit of a dual-temperature plasma with temperatures of 0.08 and 0.30 keV is also an acceptable fit. There is a considerable amount of diffuse X-ray emission protruding from the disk in the NW direction out to approximately 6 kpc. We analyse the point source population using a *Chandra* observation, using a maximum likelihood method to find that the slope of the cumulative luminosity function of point sources in the galaxy is $-0.77^{+0.13}_{-0.1}$. Using a sample of other local galaxies, we compare the X-ray and infrared properties of NGC 891 with those of 'normal' and starburst spiral galaxies, and conclude that NGC 891 is most likely a starburst galaxy in a quiescent state. We establish that the diffuse X-ray luminosity of spirals scales with the far infrared luminosity as $L_X \propto L_{FIR}^{0.87 \pm 0.07}$, except for extreme starbursts, and NGC 891 does not fall in the latter category. We study the supernova SN1986J in both *XMM-Newton* and *Chandra* observations, and find that the X-ray luminosity has been declining with time more steeply than expected ($L_X \propto t^{-3}$).

Key words: galaxies:individual: NGC 891 – X-rays: diffuse emission – galaxies: starburst – supernovae:individual: SN1986J – X-rays: galaxies

1 INTRODUCTION

The environment of a spiral galaxy can influence its evolution in many ways. Close interactions with nearby galaxies have been shown to trigger inspire star formation, and thus alter the interstellar medium (ISM) of the galaxy. Properties of the ISM could also be affected by direct infall of material from the intergalactic medium (IGM), or, if the galaxy is in a group or cluster, by the ram pressure stripping by the IGM. However, in certain, outflows into the IGM could be a significant mode of the interaction of a galaxy with its surroundings. Bursts of star formation in the galaxy can, if sufficiently strong, lead to the outflow of matter, which will be predominantly visible at H α and X-ray wavelengths (Shopbell & Bland-Hawthorn 1998; Lehnert, Heckman & Weaver 1999). These outflows can be strong enough to escape the visible extent of the galaxy, but still be retained by the halo of the galaxy. In some of these cases, the burst of star formation would be strong enough

for the outflow to be able to could escape the galaxy and its halo, and appear as a superwind.

A detailed study of the region of interface between the optical extent of the galaxy and the surrounding medium, is clearly important. Edge-on spiral galaxies, such as the galaxy we study here, NGC 891, are oriented in such a way that these are particularly useful in the study of this interface region (Strickland et al. 2004). Because of the energies associated with supernovae and the wind of massive stars, observations at X-ray energies are of particular interest in studying the hot haloes or outflows from galaxies. Of the two currently operating major X-ray missions, *Chandra* has very high spatial resolution and moderate collecting area, whereas *XMM-Newton* has reasonable spatial resolution, but a larger collecting area, and thus should be able to see lower X-ray surface brightness features.

In this paper we will present results from *XMM-Newton* and *Chandra* observations of NGC 891, an edge-on spiral galaxy. NGC 891 is very similar in many respects to our own galaxy. The high inclination makes NGC 891 ideal for studying the diffuse X-ray emission from the outflow extending from the plane of the galaxy (particularly in the NW direction), which has previously been

^{*} E-mail: rft@star.sr.bham.ac.uk ; somak@star.sr.bham.ac.uk; irs@star.sr.bham.ac.uk

studied with the *ROSAT* (Bregman & Pildis 1992), *ASCA* (Bregman & Pildis 1994; Read, Ponman & Strickland 1997) and *Chandra* (Strickland et al. 2004) observatories.

High-resolution X-ray studies reveal diffuse emission up to about 10^{37} erg s $^{-1}$, but also reveal a rich point source associated with stellar sources, such as X-ray binaries and supernovae. The X-ray point source population is closely related with the history of star formation in the galaxy (e.g., Kilgard et al. 2002). The slope of the X-ray luminosity function (XLF) of point sources is believed to be a good indicator of this, with flatter XLF slopes indicating more recent star-formation (due to a large fraction of high luminosity massive X-ray binaries). The point source populations of several nearby galaxies have been analysed (Hartwell et al. 2004; Kilgard et al. 2002; Colbert et al. 2004). Of them, Hartwell et al. (2004) selected a small group of well-studied spirals, and found that the XLF slope is generally steeper for normal spiral galaxies than for the starburst galaxies, and correlated with other observable parameters. In this work, we compare these X-ray, optical and IR properties of NGC 891 with a similar sample of normal and starburst galaxies.

As part of the point source population, the presence of an active galactic nuclei (AGN) is also the subject of much debate in NGC 891 and other galaxies, and how dominant or irrelevant the AGN is to the energetics of the central regions of the galaxy. Strickland et al. (2004) show that there is the possibility of a weak hard X-ray source (2.0-8.0 keV) using the *Chandra* data. The discovery of a nuclear AGN in NGC 891 would help us to categorise it as a starburst galaxy.

A rare form X-ray point sources in galaxies are X-ray luminous young supernovae. There have been few X-ray detections of young supernovae, and the ones that have been detected are associated with relatively nearby Type II SN events (Houck et al. (1998) and references within). One of these rare objects, detected at X-ray wavelengths, is SN1986J, located in NGC 891 and detected as a bright source in our X-ray observations. It is also very radio bright. Houck et al. (1998) studied the evolution of SN1986J using both *ASCA* and *ROSAT* data. SN1986J is still visible at X-ray energies and we present a new analysis of the evolution of this source using both *Chandra* and *XMM-Newton* data.

The paper is organised as follows: In §2 we discuss the *XMM-Newton* and *Chandra* data used here, and present the reduction procedure and results of the analysis of point sources (*Chandra*) and the diffuse emission (XMM) in §3. In §4, a comparison of X-ray and near and far-IR properties is made with other nearby spiral galaxies. Observations of the supernova SN1986J are presented in §5, and compared with observations at previous epochs. General conclusions are presented in the final section.

2 OBSERVATIONS

NGC 891 is similar to the Milky Way in optical luminosity ($m_B^{0,i} = 9.4$ from RC3, implying $M_B = -20.4$), Hubble type (Sb) and rotational velocity (225 km s $^{-1}$, van der Kruit 1984; Rupen 1991). It is a nearby edge-on spiral, and thus has been the subject of many detailed studies of interstellar dust and gas, from observations of the radio contin-

Table 1. The nearby edge-on spiral galaxy NGC 891.

Parameter	Value
RA (h m s)	02:22:33.41
DEC ($^{\circ}$ ' ")	+40:20:56.9
Diameter (major)	14.1'
Diameter (minor)	3.1'
Major-axis position angle	22 $^{\circ}$
Redshift	528 km/s
Adopted Distance	9.08 ± 0.45 Mpc

Notes: RA and Dec are given in J2000. The diameters correspond the D_{25} ellipse (i.e. the length of the axis at the isophotal level of 25 mag/arcsec 2 in the B Band) Source: *NED*, *LEDAS*. Source of distance explained in §2.

uum (e.g., Dahlem, Dettmar, & Hummel 1994), H I (e.g., Swaters, Sancisi, & van der Hulst 1997), carbon monoxide (e.g., Sofue & Nakai 1993) and molecular hydrogen (e.g., Valentijn & van der Werf 1999).

However, there is considerably more star formation in NGC 891 than in the Milky Way, presumably due to the presence of about 2.5 times as much molecular gas (Scoville et al. 1993). As a result, NGC 891 is found to be twice as luminous at IR wavelengths (Wainscoat, de Jong & Wesselius 1987), and there is evidence of enhanced dust extinction for optical light, even outside the plane (e.g., Howk & Savage 1997). The extended gaseous halo of the galaxy is evident from $H\alpha$ observations using HST/WFPC2, with filaments reaching up to 2.2 kpc above the galactic plane (Rossa et al. 2004).

Other wavelengths have yielded other interesting details. Polarised radio emission has been detected from NGC 891 (Sukumar and Allen 1991), illustrating the nature of the interstellar magnetic field. A luminous radio halo has been well established with a scale height of 2.7 kpc (Allen, Baldwin & Sancisi 1978).

Throughout this analysis, we assume a distance of 9.08 ± 0.45 Mpc for NGC 891, which is a weighted mean of the values obtained by Ciardullo, Jacoby & Harris (1991) and Tonry et al. (2001)). Other selected parameters are shown in Table 1. Where relevant, we use $H_0 = 72$ km s $^{-1}$ Mpc $^{-1}$.

2.1 XMM-Newton observations

NGC 891 was observed with the *XMM-Newton* telescope on August 22 2002, as part of a GTO observation. The galaxy was at the centre of the field of view, with the entire emission also contained within the field of view.

The *XMM-Newton* data was observed with three different cameras, MOS1, MOS2 and PN. Each of the data sets were analysed separately. After running the standard SAS tasks: CIFBUILD and ODFINGEST; the chains to process the *odfs* were run (EMCHAIN, EPCHAIN) simultaneously running the BADPIXFIND command. These have proved to be considerably better at detecting bad pixels than the tasks EMPROC and EPPROC. Having extracted the lightcurve in the 10–15 keV energy range, the observation was found to contain a considerable amount of flaring which we used to identify the good time intervals. The periods of high background

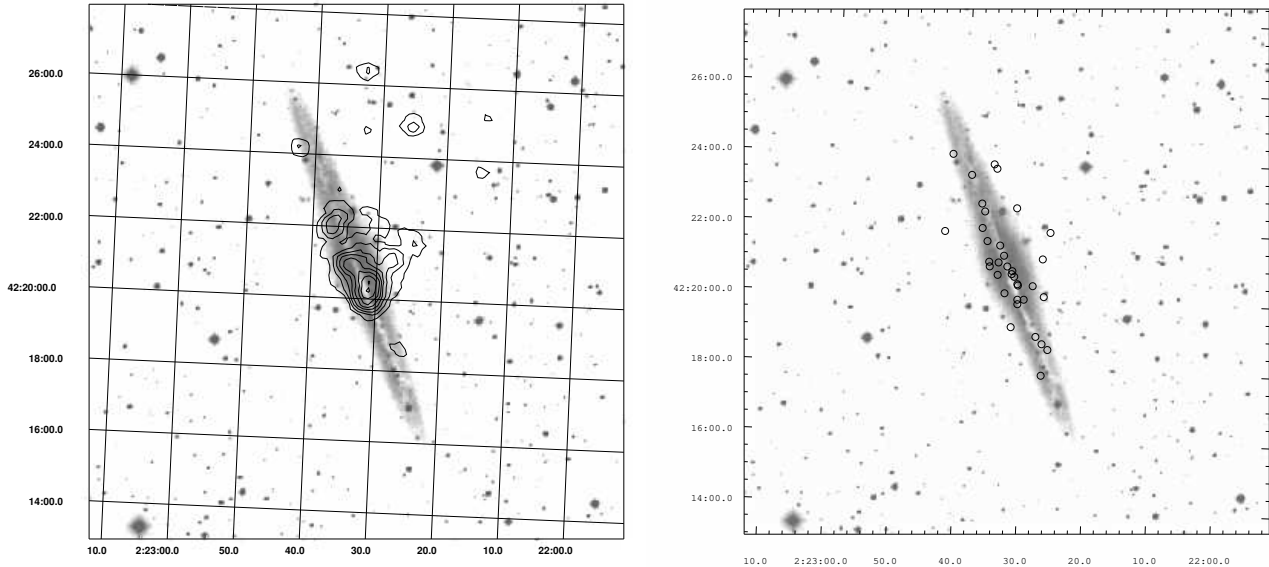


Figure 1. a): The *XMM-Newton* soft X-ray (0.3–2.0 keV) contours overlaid onto the optical Digitised Sky Survey (DSS) image. The lowest contour level is set at 3σ above the background. b): point sources.

were identified by eye at 55/40.0 counts for the MOS/PN cameras respectively. The resulting good times are 14.6 ks (originally 18.0 ks) for MOS1/MOS2; and 9.6 ks (originally 15.0 ks) for PN.

Events were filtered based on the the pattern parameter, which indicates the geometry of the detection of each event, i.e. the number of adjacent pixels that detect each photon. The events that were retained in the filtering were the ones that are well-calibrated (singles, doubles and quadruples for MOS & singles and doubles for PN). Due to the extent of the diffuse emission present in this galaxy, we used blank sky background files for subtraction of our data. We followed the technique set out by Read & Ponman (2003) for producing images and spectra that are correctly background subtracted.

Given the high density of point sources, and the high inclination, it seemed that manually setting a region with exclusion regions based around the point sources (extracted from *Chandra* data— see below) was more appropriate. The radius of the exclusion region was set by the SAS task CALVIEW, using the encircled energy (PSF) function, at $15''$ (corresponding to a PSF fraction of 75%). When the sources were removed, we used the CIAO task DMFILTH to interpolate over the holes. The width of the background annuli were initially taken to be 1.5 times the radius of the source region, but many were adjusted to ensure that the background annuli did not overlap with any source regions. In some cases it was impossible to extract adequate background annuli due to the compact nature of the sources on each other. In that case, the sources were merged and treated as a single source removal region. When analysing the spectral data, the data from the three cameras were fitted simultaneously together to ensure the best fit. However, for the radial profile analysis, the data was mosaicked together using the task EMOSAIC.

2.2 Chandra observations

To better characterise the point sources, we used the archived *Chandra*/ACIS-S observation (51 ks, PI: Bregman), which was reduced in a similar way, using the CIAO software with online threads. Once the *Chandra* data preparation was completed, the CIAO tool WAVDETECT was run on the *Chandra* data. We narrowed down the returned list of sources by excluding all the sources outside the D_{25} ellipse (see Table 1), and considering only the sources inside. We used the wavelet scales 1, 2 and 4 to extract the point sources, as these provided the best identification of all the point sources present. These sources are shown on a DSS overlay in Fig. 1). We used the results to generate an X-ray flux of each source to generate a luminosity function (Fig. 2).

3 ANALYSIS OF THE X-RAY OBSERVATIONS

Here we analyse the X-ray observations described in the previous section to characterise the population of point sources in NGC 891, using the archived *Chandra* data set, utilising the superior resolution of *Chandra*/ACIS setup. We use this observation to subtract the point sources from the XMM-Newton observation, to investigate the nature of the diffuse emission.

3.1 The Point Source Luminosity Function from Chandra

We detected a total of 26 point sources within the D_{25} ellipse, down to a flux limit of 10^{-15} erg cm $^{-2}$ s $^{-1}$, which at the adopted distance of NGC 891 amounts to a luminosity of $F_{min} = 10^{37}$ erg s $^{-1}$. The regions were all output as ellipses containing 99.7% (3σ) of the source counts. As a considerable number of the sources contained few counts, an accurate spectral fit was not possible, so we modelled each

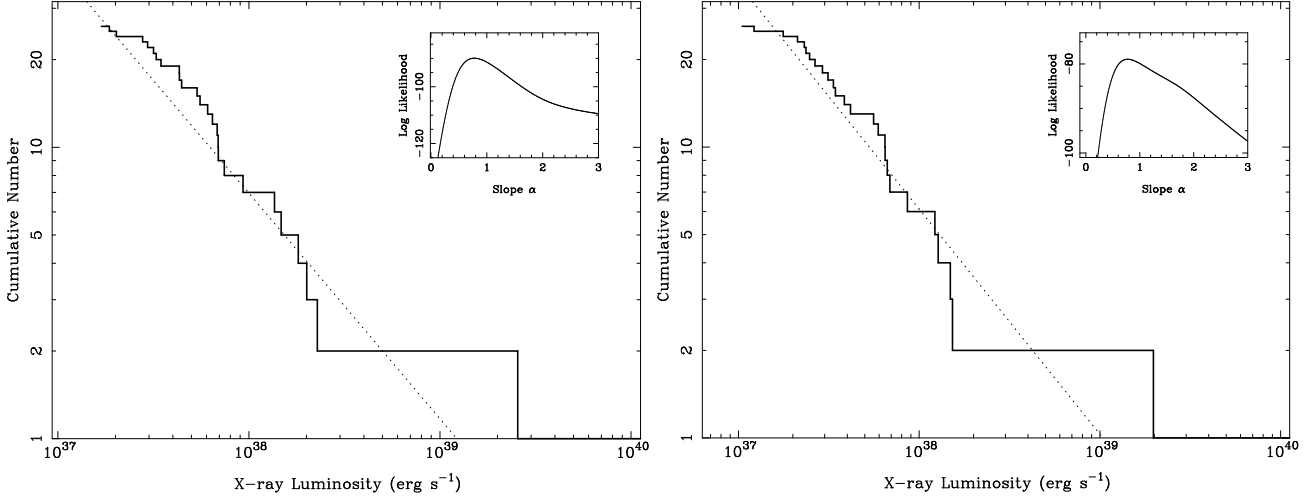


Figure 2. The X-ray luminosity function (XLF) for point sources, in NGC 891, in the 0.3–8 keV (left) and 2–8 keV (right) energy ranges, measured from the Chandra observation. The slope, defined in (1), is calculated to be $\alpha = 0.77^{+0.13}_{-0.10}$ and $\alpha = 0.77^{+0.16}_{-0.12}$ respectively. Since the slope does not substantially change for the higher energy range, we conclude that differential extinction within the inclined spiral does not significantly affect the shape of the XLF. The inset in each plot shows the shape of the log likelihood function, derived from the method of evaluating the slope and errors, discussed in §3.1.

of the point sources individually in XSPEC using an absorbed power-law model with a slope of $\Gamma = 1.8$. The point sources with more than 100 counts were individually fitted. Flux values were established for each of the point sources in an energy range of 0.3–8.0 keV, and these were combined to make a luminosity function (Fig. 2). We discuss the point source associated with SN1986J in greater detail in the following section.

As we will see below, the slope of the luminosity function can be used as an indicator of recent star formation activity in a galaxy. This so-called log N –log S relation is usually expressed in the cumulative form

$$\log N(> S) = -\alpha \log S + \kappa \quad (1)$$

where a straight line is fitted to the cumulative histogram. Here we adopt a more robust method of measuring the slope of the luminosity function with the potential of better measuring the uncertainty of the slope. This is a generalised version of the much-used method adapted from Crawford, Jauncey, & Murdoch (1970) and Murdoch, Crawford, & Jauncey (1973), the crucial difference being that in the former, errors in flux measures are not taken into account and in the latter, all errors are considered equal.

Here, each of our n point sources has a measured luminosity F_i , given the adopted distance to the galaxy, and an independently estimated error σ_i . We represent the probability distribution of the luminosity S of point sources in the galaxy in its differential form

$$P(S) dS = AS^{-\beta} dS. \quad (2)$$

On comparison with (1), $\alpha = \beta - 1$. Our exercise thus consists of maximising the log likelihood function

$$\mathcal{L} = \sum_{i=1}^n \ln P(F_i, \sigma_i), \quad (3)$$

where the distribution of our measured values of flux and standard deviation (F_i, σ_i) is given by

$$P(F_i, \sigma_i) = \frac{\int_0^\infty P(F_i, \sigma_i | S) P(S) dS}{\int_{F_{\min}}^\infty \int_0^\infty P(F_i, \sigma_i | S) P(S) dS dF}. \quad (4)$$

Assuming the errors of measuring flux and luminosity are distributed as a Gaussian, the integrand above is given by

$$P(F_i, \sigma_i | S) P(S) dS = \frac{A}{\sigma_i \sqrt{2\pi}} S^{-\beta} e^{-(F_i - S)^2 / 2\sigma_i^2} dS. \quad (5)$$

We numerically find the value of β (thus α) for which \mathcal{L} in (3) is maximum. For large N , the probability distribution for β is asymptotically Gaussian, and the 1σ error in β corresponds to $\Delta\mathcal{L} = 0.5$. For our limiting 0.3–8 keV luminosity, $F_{\min} = 10^{37} \text{ erg s}^{-1}$, we find the slope of the cumulative LF given by (1) to be $\alpha = 0.77^{+0.13}_{-0.10}$, as shown in Fig. 2.

Since NGC 891 is almost exactly an edge-on galaxy, the effect of differential local extinction might be important within the point source population, which might lead us to progressively miss the fainter objects on the far side of the galaxy. Since the effect of such extinction is energy-dependent (being larger at lower energies, particularly below 2 keV), we tested whether it is substantial by recalculating the luminosity function for the energy range 2–8 keV (Fig. 2b). The slope was found to be the same at $\alpha = 0.77^{+0.16}_{-0.12}$, leading us to conclude that the effect of differential extinction is not very serious for this target.

3.2 The diffuse X-ray emission from XMM-Newton

We extracted the spectrum of the diffuse emission in the energy range 0.3–6 keV, excluding a circle of 15 arcsec around each detected point source, from the 3 XMM-Newton camera data and analysed them with the *heasoft* package XSPEC. We performed simultaneous fitting of all three data sets in order to fit the best model. We also tried to add the Chandra diffuse emission to the fits, but due to the lim-

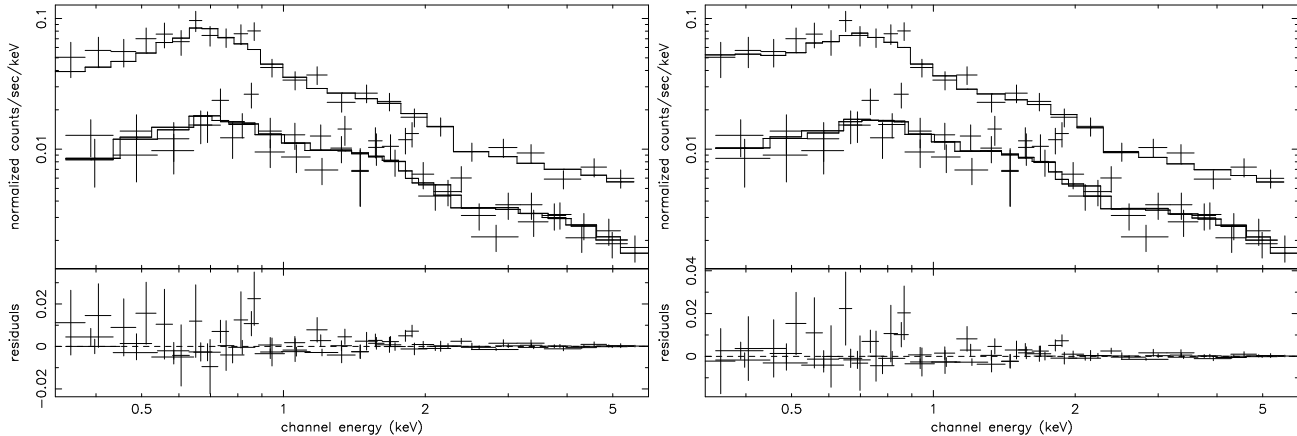


Figure 3. (a): The X-ray spectra of NGC 891, with an absorbed single temperature model + power law. Spectra for all three XMM-Newton cameras have been simultaneously fitted in the 0.3–6.0 keV energy range. The top spectrum is from the PN camera. (b): As in (a), but the fitted model is an absorbed dual temperature + power law.

Table 2. Summary of recent fits to the diffuse X-ray emission. The XMM-Newton data are the results generated from this work.

Obs.	Model	kT_1 (keV)	kT_2 (keV)	χ^2_{red}
XMM	pow+mek	0.26 ± 0.01	-	1.06
XMM	pow+mek+mek	0.08 ± 0.01	0.30 ± 0.03	1.05
ROSAT ^a	mek+mek	0.31	10	-
ROSAT ^b	mek	0.11 ± 0.03	-	1.10

Notes: References: a) Bregman & Pildis (1994), b) Read, Ponman & Strickland (1997)

ited collecting area of the *Chandra* telescope, we found the diffuse emission spectra generated did not improve the fit.

We initially fitted an absorbed single temperature plasma model with a power-law component to the data. We fixed the Galactic value of column density n_H of $6.78 \times 10^{20} \text{ cm}^{-2}$ (obtained from *Colden*). Since the target is an edge-on galaxy, the local column density is expected to be substantial- this was looked for, and fixed at a fairly low value of n_H (local) at $2.0 \times 10^{19} \text{ cm}^{-2}$. The power-law model was added to our data to account for point source contamination.

Figure 3a shows the best fit to all three data sets, having a $\chi^2=68.35$ with 65 d.o.f., leading to $\chi^2_{red}=1.06$. We extract a value of $kT = 0.26 \pm 0.01 \text{ keV}$. In comparison, Read, Ponman & Strickland (1997) fit a single temperature model to the data with a cooler temperature component ($0.11 \pm 0.03 \text{ keV}$). Bregman & Pildis (1994) found that the data was best fitted by a two-temperature model with kT at 0.31 and 10 keV.

As the result from Bregman & Pildis (1994) implied a two temperature model, a second temperature component was added to the data (Fig. 3b). The two temperatures that were inferred, as a result, were $kT = 0.08 \pm 0.01 \text{ keV}$ and $0.30 \pm 0.03 \text{ keV}$. The two temperatures agree within errors to the cooler temperature component derived by Bregman & Pildis (1994) and the single temperature component derived by Read, Ponman & Strickland (1997).

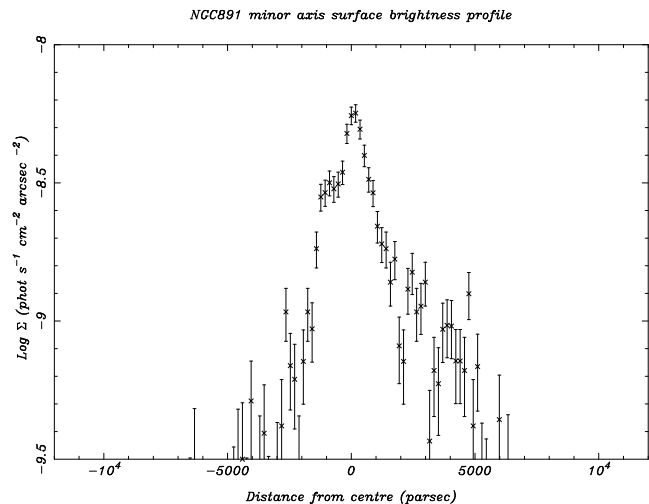


Figure 4. Minor axis radial surface brightness profile of the diffuse emission. The plot is in the 0.3–8.0 keV energy band.

However, it should be stated that the spectrum of the data was best constrained by a single temperature fit, and the improvement in the χ^2_{red} by adding a second temperature component is not statistically significant (f-test statistic value = 1.05).

A summary of our fit parameters compared with those of Bregman & Pildis (1994) and Read, Ponman & Strickland (1997) are presented in Table 2.

Our results do seem to complement the *ROSAT* data to some extent. Our single and dual temperature model values are consistent with temperatures that both have derived. Bregman & Pildis (1994) do find a high temperature component at 10 keV, which is not determined from our fits. The reason for this may be the poor resolution of *ROSAT*, which means that it is difficult to remove point sources effectively. This effect is compounded by the high inclination of the system. Also, SN1986J was considerably brighter, at the time of the *ROSAT* observation more than ten years ago, than it is now, and may well have contaminated the extracted diffuse emission. Finally, the hard X-ray flux of a nearby unresolved

bright point source near SN1986J might also account for this discrepancy (Read, Ponman & Strickland 1997).

We also extracted images of the diffuse emission from the *XMM-Newton* data. These images complement the X-ray observations from *ROSAT* (Bregman & Pildis 1994) and *Chandra* (Read, Ponman & Strickland 1997). There is a considerable amount of emission from the centre of the galaxy in the NW direction. Figure 1a shows this result for the soft energy band (0.3–2.0 keV). The X-ray contours are overlaid onto the optical Digitised Sky Survey (DSS) image. The image was smoothed with an adaptive gaussian program ASMOOTH such that the 1σ width of the gaussian contained 40/3 counts around each pixel. We also took a minor axis diffuse emission profile to show the extent over which the extended emission protrudes (Fig. 4). The emission protrudes out to just over 6 kpc from the centre of the galaxy in the NW direction, but drops off rapidly in the SE direction outside the plane of the galaxy.

3.3 Evidence of central AGN

Using the *Chandra* observation, Strickland et al. (2004) found a weak hard (2.0–8.0 keV) X-ray source near the nucleus of the galaxy, defined as the position of the radio continuum point source (Rupen 1991). This was suggested to be a weak AGN possibly associated with the radio source. Unfortunately, we were not able to detect this source with our *XMM-Newton* observation, most likely due to the poorer resolution compared to *Chandra*.

4 COMPARISON WITH OTHER LOCAL GALAXIES

In order to characterise the global properties of NGC 891 and find whether its properties are consistent with that of a starburst galaxy or not, we compile various X-ray, near-IR and far-IR properties of several nearby spiral galaxies, of which some are normal galaxies and some are actively star-forming and starburst galaxies. Starting from a sample of galaxies selected from Hartwell et al. (2004), a few galaxies from Strickland et al. (2004) and Hartwell et al. (2004). A selected list of parameters are collected in Table 6.

Far-Infrared luminosities We calculated the FIR luminosities (erg s^{-1}) differently depending on whether the source was from *ISO* (preferably) or *IRAS*. We used the equations from Bendo et al. (2002) (fluxes in Jy):

$$L_{\text{FIR}} = 1.89 \times 10^{-14} (1.36f_{60} + 0.958f_{100} + 0.439f_{180}), \quad (6)$$

and for *IRAS*

$$L_{\text{FIR}} = 1.26 \times 10^{-14} (2.58f_{60} + f_{100}), \quad (7)$$

Near-Infrared luminosities To calculate the K-band luminosity L_K (erg s^{-1}), we derived the following expression using the zero point values from Cohen, Wheaton & Megeath (2003) :

$$\log L_K = 43.13 - 0.4K_{\text{tot}} + 2 \log D, \quad (8)$$

with D in Mpc, and K_{tot} the total K-band magnitude taken from the 2MASS galaxy atlas (Jarrett et al. 2003).

X-ray luminosities L_X was established from the literature, but different authors used varying energy ranges. Strickland et al. (2004) evaluate their fluxes for an energy range 0.3–2.0 keV (soft X-ray). We have adopted this energy range to keep our values for L_X . In the case where the data was not in the necessary energy range, we used the Portable Interactive Multi-Mission Simulator (PIMMS) to generate our data. Using the model fit parameters for the diffuse emission in the literature, we estimated a revised flux in the appropriate energy range.

Deprojected area of galaxy We differ from the calculation made by Hartwell et al. (2004) for the area of the D_{25} ellipse. Hartwell et al. (2004) calculated the galaxy area as $\pi ab \cos \theta$. For systems that are face on (such as NGC 4214) this calculation is adequate. However, for very high inclination systems, the measure of the semi-minor axis simply represents the width of the disk, and cannot be used in calculating the area. Therefore, for the sake of consistency we choose to evaluate our area as πa^2 for all galaxies in our sample.

4.1 Starburst or not?

There has been much discussion as to whether NGC 891 is a normal spiral galaxy, or whether it is a starburst (Strickland et al. 2004). We try to categorise NGC 891 by means of comparison with a sample of 16 nearby galaxies. Figure 5 contains four plots, which are described below.

The slope of the luminosity function can be used as an indicator of the general properties of the host galaxy. If the star formation rate in the galaxy is constant, then the luminosity function of the sources should be fit by a single unbroken power-law model. If the galaxy is a starburst one, then new high mass X-ray binaries (HMXBs) would be formed, breaking the luminosity function slope. The break in the slope would decrease with time, and would be an indication of the time of previous bursts in the galaxy.

As we saw above, in NGC 891, we chose to fit the XLF slope can be fitted by a single power-law. In the case of NGC 1482, the galaxy is further away (22 Mpc) and only two sources could be detected so no XLF slope was determined. Two other galaxies NGC 4244 and NGC 6503 also have low statistics (with 3 and 4 sources respectively), but XLF slopes were calculated by Colbert et al. (2004). We include these in our plots, but they do not appear to be representative of the normal spirals category.

Figure 5a plots the XLF against the S_{60}/S_{100} flux ratio. Lehnert & Heckman (1996) analyse the properties of superwinds and quantitatively discuss the likelihood of generating a superwind with respect to the infra-red properties of the galaxy. The galaxies with high luminosity ($L_{\text{IR}} \geq 10^{44} \text{ erg s}^{-1}$), large infra-red excesses ($L_{\text{IR}}/L_{\text{OPT}} \geq 2$) and warm far infra-red colours ($S_{60}/S_{100} \geq 0.5$) are most likely to have galactic superwinds. For the sample selected, the last criterion is satisfied for all the starburst galaxies. Of the starburst galaxies in our sample, superwinds are detected in M82 (Strickland et al. 1997), NGC 253 (Strickland et al. 2000) and NGC 4945 (Moorwood et al. 1996). NGC 5253 (Strickland & Stevens 1999) and NGC 4449 (Summers et al. 2003) exhibit emission from superbubbles. Although superwinds and superbubbles are both the result of massive star

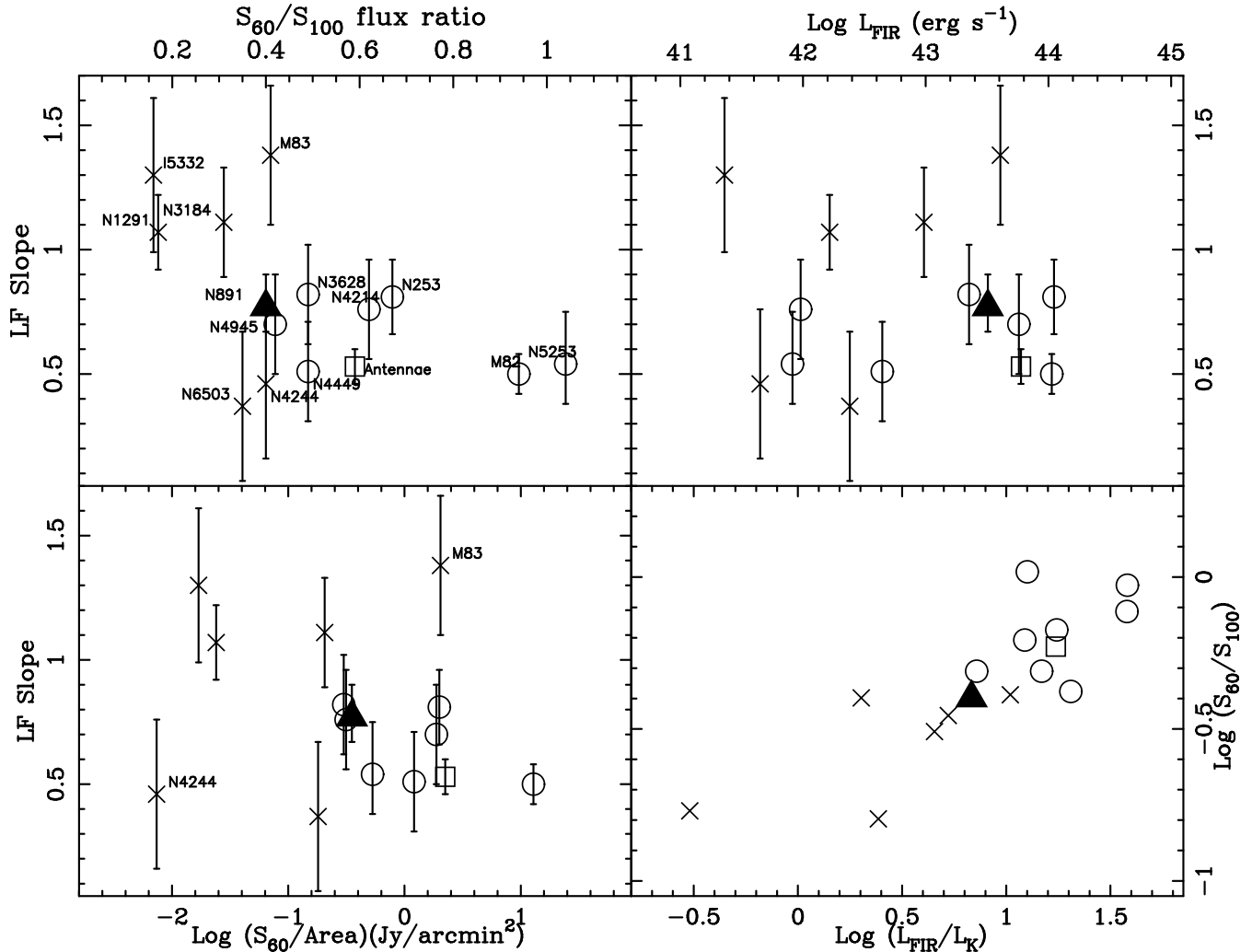


Figure 5. Top left a): the XLF slope plotted against the *IRAS* flux ratio S_{60}/S_{100} for a sample of nearby galaxies. The circles represent starburst galaxies; crosses represent normal spirals; square for interacting galaxies; and the filled triangle represents NGC 891. The same symbols are used throughout this paper. The data labels have been removed for all other plots for neatness. The only labels left in are those referred to in the text. The error on NGC 891 is the standard deviation, discussed in §3.1. Top right b): the XLF plotted against far infra-red luminosity L_{FIR} . Bottom left c): the XLF plotted against the ratio of the *IRAS* 60μ flux and the spiral galaxy area. Bottom right d): the *IRAS* flux ratio plotted against L_{FIR} normalised with the K-band luminosity.

formation processes within the densest regions of the hot galaxies, the winds are able to channel the metals produced straight into the IGM, whereas the superbubbles do not reach the outskirts of the host galaxies, hence retaining their newly processed metals, consequently raising the abundance of the ISM (Tenorio-Tagle, Silich & Muñoz-Tuñón 2003). The only starburst galaxies not to have superwinds or superbubbles are NGC 4214, which is calculated likely to exhibit blowout (Hartwell et al. 2004) and the Antennae, which is an interacting system, so no superwind has formed due to disruption from the merging.

Therefore, there are two distinct categories of result: The low XLF slope galaxies have a higher ratio of warm IR colours than the high XLF slope galaxies, which are normal spiral galaxies. NGC 891 appears to have the XLF slope of a starburst, but the S_{60}/S_{100} corresponding more to normal spirals than starbursts.

Figure 5b plots the far infra-red luminosity (L_{FIR})

against the XLF slope of the data. L_{FIR} is an indicator for how much dust there is in a galaxy, and hence the star formation rate (Kennicutt 2003). The FIR also contains the most important cooling lines in the neutral ISM. Therefore, if the XLF slope is dependent on star formation rate, then, one would expect a correlation between these two parameters. However, this is not observed in our sample. Both the starbursts and normal galaxies span a wide overlapping range of FIR luminosities. The division between spirals and starbursts is quite clear in this plot, breaking either side of 1. Therefore, an XLF- L_{FIR} dependence cannot be justified on the basis of these results.

Figure 5c plots the XLF slope against the S_{60} flux scaled against the area of the D_{25} ellipse. The x-axis therefore represents the star formation rate per unit area. There is a definite correlation between the data points on this plot. The higher star formation rate corresponds to starburst galaxies, which we would expect to see. The major exceptions to this trend

are NGC 4244 and M83. The XLF slope of NGC 4244 was determined with only three data points (Colbert et al. 2004), and has an estimated error on the data. M83 should be classified as a starburst, as observations indicate that there are massive clusters of stars in the nuclear region (Harris et al. 2001). However, as discussed in Kilgard et al. (2002) the star formation rate is low compared to other starbursts, and the starburst region is confined to a small area of the galaxy. Therefore, most of the point sources analysed were taken from a region outside of the starburst region, so the XLF slope is more representative of the disk population of normal spirals as opposed to the standard starburst population.

In Fig. 5d, the warm IR colour ratio S_{60}/S_{100} is plotted against the ratio of L_{FIR}/L_K . This ratio tells us the extent of the star formation activity normalised against the stellar types present in the galaxies. The different galaxy types are clearly grouped separately, and all the galaxies seem to follow a linear trend. The normal spiral galaxies have lower star formation rates, which would imply that they are less likely to generate galactic superwinds. The galaxies with higher star formation rates are all starburst galaxies with superwinds (or superbubbles) present. Again, NGC 891 seems to sit between the two categories, making it difficult to categorise as either a spiral or as a starburst.

4.2 The X-ray Schmidt law

In a classic paper, Schmidt (1959) showed that the rate of Population I star formation is proportional to the density of available gas in a galaxy. This has been re-discovered in various guises over the last few decades. In terms of the X-ray luminosity of the galaxy, which is related to a density of hot gas, one expects it to correlate with the star formation rate, which we can characterise by the total far-IR flux.

Ranalli, Comastri & Setti (2003) analyse the effectiveness of the 2–10 keV X-ray luminosity as a star formation rate indicator, showing the linear relation between the X-ray luminosity and the far-IR luminosities, although there are discrepancies between many other published results. Previous studies using *ASCA*, *ROSAT*/*PSPC* or *EINSTEIN* values would overestimate L_X , being unable to separate out the emission from X-ray binaries and AGN.

Griffiths & Padovani (1990) established $L_X \propto L_{FIR}^{0.6}$, although S_{60} made up the x-axis, and L_X ranged from 0.5–3.0 keV. Also with the *EINSTEIN* satellite, David, Jones & Forman (1992) obtained an almost linear fit to their data $L_X \propto L_{FIR}^{0.95 \pm 0.06}$ agreeing quite well with our results within errors. This result was determined in the 0.5–4.0 keV energy band and the sample was a selection of starburst and normal galaxies. Ranalli, Comastri & Setti (2003) analyses data obtained from the *ASCA* satellite and for a soft X-ray energy range of 0.5–2.0 keV obtains $L_X \propto L_{FIR}^{0.87 \pm 0.08}$, an identical result to ours for a very similar energy range (we use 0.3–2.0 keV).

We plot L_X (the diffuse X-ray luminosity) against L_{FIR} for our sample galaxies in Fig. 6. We establish that the relation between the data is $L_X \propto L_{FIR}^{0.87 \pm 0.07}$, without the two data points on the plot which do not appear to lie near the line. If these are included, the fit becomes considerably worse: $L_X \propto L_{FIR}^{0.71 \pm 0.12}$. These are the two starburst galaxies NGC 253 and NGC 4945, both of which contain a superwind emitting from the centre. This would indicate the presence

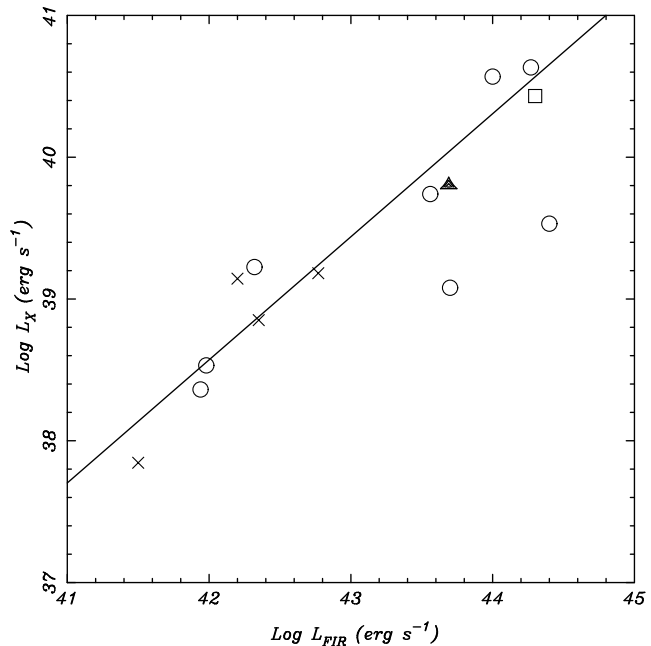


Figure 6. The X-ray Luminosity against IR luminosity for a sample of galaxies. The circles represent starburst galaxies; crosses represent normal spirals; the square for interacting spirals; and the filled triangle represents NGC 891.

of an excess of dust in these galaxies containing considerable star formation.

NGC 891 lies comfortably near the best-fitting line, away from the normal galaxies since its X-ray and far-IR fluxes are higher, again showing that it does not have as extreme a rate of star formation as a starburst galaxy.

5 THE RESIDENT YOUNG X-RAY SUPERNOVA SN1986J

Even though thousands of supernovae have been found in the optical, there are instances of only 15 supernovae being detected in the X-ray (Immler & Lewin 2003; Bregman et al. 2003). Of these, a handful have been monitored over many years, their X-ray emission dominating their radiative output after about a year after explosion (Pooley et al. 2002). Thermal emission from the reverse shock region is expected to be seen as softer X-ray emission within the expanding SN shell as it interacts with the dense stellar wind of the progenitor (Chevalier & Fransson 1994).

One of these Type II supernovae observed in the X-rays is SN1986J in NGC 891, which was discovered using radio observations from the VLA (Rupen et al. 1987). The first X-ray observations of SN1986J were taken with *ROSAT* (Bregman & Pildis 1992). Since then, two more *ROSAT* and two *ASCA* observations have been undertaken in the mid 1990's (Houck et al. 1998). The X-rays are thought to be caused by a shock propagating through the former stellar envelope (Bregman & Pildis 1992); or due to the supernova envelope colliding with a shocked clumpy wind, which produces the X-rays (Chugai 1993). Bregman & Pildis (1992) found that the X-rays were emitted primarily in the soft

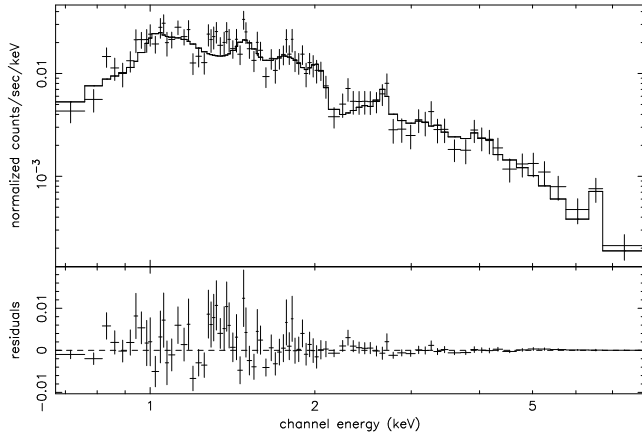


Figure 7. The *Chandra* X-ray spectrum for SN1986J.

X-ray band (0.1–2.5 keV). An analysis of the *ROSAT* and *ASCA* observations was done by Houck et al. (1998), who determined that the X-ray light curve of the data was dropping by t^{-2} , which was considered to be a rather fast decline.

A summary of all observations are shown in Table 3. Note that the X-ray fluxes derived for the *ASCA* data are an average over all their different models, and so the error shown here is simply the standard deviation of these data sets.

5.1 The spectrum of SN1986J

The spectrum for the *Chandra* observation was extracted using a local background and we fitted different temperature models to the data. Firstly, an absorbed single temperature thermal plasma model (MEKAL) was fitted with a local and Galactic absorbing column (Bregman & Pildis 1992). The Galactic value for $\log n_H$ was fixed at 20.8 (n_H in cm^{-2}) and the local absorbing column was allowed to vary. The abundance was initially fixed at 0.3 then 1.0 solar, and finally was allowed to vary. The local $\log n_H$ was evaluated at 21.6, in good agreement with the value of Bregman & Pildis (1992) (21.7), but the temperature range that we obtained from the model was 3.5–4.1 keV. This temperature component is much larger than the 2.0 keV values obtained from the *ROSAT* observations, but smaller than the *ASCA* temperature ranges. A VMEKAL model was also tried, where the individual element abundances are allowed to vary, as the mekal fit results were leaving several emission lines unidentified. The result from the vmekal fit is plotted in Fig. 7. The temperature was determined to be 4.6 keV, local $\log n_H = 21.5$, and X-ray flux $0.45^{+0.1}_{-0.7} \times 10^{-14} \text{ erg s}^{-1} \text{ cm}^{-2}$. Many elements were identified in the spectrum of the supernova, most notably, the Fe emission line at 6.4 keV. The abundances are tabulated in Table 4.

On inspection of Fig. 7, some of the emission lines are not fitted that well by a VMEKAL model. Several methods were tried to improve the fit, including a two temperature model (MEKAL+VMEKAL) and a different single temperature thermal plasma model (APEC). In each of these models, the hard temperature and local n_H were similar to the results obtained from the single temperature fitting. For the two temperature fitting, the lower temperature component was 0.11 keV which is likely the component from the diffuse emis-

Table 3. Summary of X-ray observations of SN1986J.

Telescope (1)	Date (2)	MJD (3)	Flux (4)
<i>ROSAT</i>	Aug 1991	48486.1	7.90 ± 0.41
<i>ROSAT</i>	Jul 1993	49206.5	4.91 ± 0.24
<i>ASCA</i>	Jan 1994	49374.5	6.07 ± 0.13
<i>ROSAT</i>	Jan 1995	49744.0	3.95 ± 0.26
<i>ASCA</i>	Jan 1996	50113.5	5.28 ± 0.10
<i>Chandra</i>	Nov 2000	51852.0	$0.96^{+0.05}_{-0.06}$
<i>XMM-Newton</i>	Aug 2002	52508.0	0.85 ± 0.15

NOTES: Column (1): The first 2 *ROSAT* observations were taken with the PSPC, the last with the HRI. Column (4): The X-ray fluxes are measured in $10^{-13} \text{ erg s}^{-1} \text{ cm}^{-2}$. The *ASCA* and *ROSAT* data are compiled from Houck et al. (1998); the *Chandra* and *XMM-Newton* fluxes are from this paper.

Table 4. Metal abundances for single VMEKAL model.

Metal	Abundance
Ne	5.12
Mg	2.71
Al	5.42
Si	1.87
S	3.8
Ar	1.09
Ca	3.48
Fe	0.92

NOTES: Abundances are relative to solar.

sion of the galaxy, and not the supernova. The results from all the *Chandra* fits are tabulated in Table 5. None of the fits identified any of the other emission lines. As all the flux values generated from the fits were similar, the value adopted for our supernova flux is the weighted mean of the different models: $9.6^{+0.6}_{-0.4} \times 10^{14} \text{ erg s}^{-1} \text{ cm}^{-2}$. The energy range chosen was 0.5–2.5 keV to be consistent with the energy ranges used in the *ASCA* and *ROSAT* data.

For the *XMM-Newton* data, the flux was much harder to determine. As the flux is dropping every year, the supernova becomes harder to model the later the observations are. We fitted all three cameras simultaneously to try and obtain the best fit to the data. Our data was best fitted with a single temperature model (MEKAL) with a temperature of 3.6 keV and absorbing column density $\log n_H = 21.53$. This fit resulted in a flux of $8.31 \pm 1.06 \times 10^{14} \text{ erg s}^{-1} \text{ cm}^{-2}$. Fitting a dual temperature model did not improve the fit. The temperatures obtained from the fit were 0.21 keV and 3.82 keV for the soft and hard components respectively. This fit did produce a surprisingly large local n_H of 22.6. The two-temperature flux was $8.40 \pm 1.16 \times 10^{14} \text{ erg s}^{-1} \text{ cm}^{-2}$. The value adopted from the flux is the mean of the four different temperature fits for the *XMM-Newton* data: $8.5 \pm 0.15 \times 10^{14} \text{ erg s}^{-1} \text{ cm}^{-2}$.

5.2 The evolution of SN1986J with time

SN1986J has been observed with *ROSAT*, *ASCA*, *Chandra* and *XMM* over the last twelve years. In Fig. 8 we plot the

Table 5. XMM and Chandra single-temperature fits to the supernova lightcurve.

Telescope (1)	Model (2)	kT (3)	nH (4)	Flux (5)	χ^2_{red} (6)	Abund (7)
Chandra	mek	3.5	0.41	9.7	1.34	0.3F
Chandra	mek	4.0	0.39	9.6	1.16	1.0F
Chandra	mek	4.1	0.39	9.7	1.15	1.30
Chandra	vmek	4.6	0.30	9.5	1.09	-
Chandra	mek+vmek	4.6	0.34	9.5	1.13	-
Chandra	apec	4.0	0.39	9.9	1.39	1.48
Chandra	vapec	4.1	0.37	9.6	1.18	-
Chandra	apec+vapec	5.9	0.45	9.5	1.16	-
XMM	mek	3.6	0.35	8.3	0.92	0.77
XMM	apec	3.4	0.37	8.6	0.92	0.77
XMM	vmek	3.8	1.15	8.4	0.90	-
XMM	mek+mek	4.2	0.38	8.7	0.84	-

NOTES: Col (3): Temperature component of the supernova fitting in keV. For two-temperature models this is the harder component. Col (4): Absorbing column parameter local to NGC891 $\times 10^{22} \text{cm}^{-2}$ Col (5): X-ray flux $\times 10^{-14} \text{erg s}^{-1} \text{cm}^{-2}$. Col (7): Abundance (relative to solar) from different fitting models. 'F' indicates a fixed fitting value. These are not shown for the vmekal/vapec model.

0.5–2.5 keV flux against time over this period. We recall that from the ROSAT and ASCA data (Houck et al. 1998), the decline of this flux was found to be $\propto t^{-2}$, which was considered to be rather steep.

Here we attempt to find a mean rate of decline over a much larger time scale. The data from ASCA and ROSAT appear to be inconsistent (Houck et al. 1998) and so we have established a best fit line inclusive and exclusive of the ASCA data. The slopes are calculated as -2.99 ± 0.45 and -2.89 ± 0.19 respectively. In Fig. 8, we also show an alternative set of points for ASCA where we attempt to correct for the poor resolution by subtracting from the the flux of the SN the combined flux of all the other point sources that are expected to be within its point-spread function.

However, our results imply $L_X \propto t^{-3}$. We can compare this with the expected behaviour from the work of Chevalier & Fransson (1994), who show that $L_X \propto t^{-1}$ when free-free emission dominates ($T > 4 \times 10^7 \text{K}$), and $L_X \propto t^{-0.7}$ when line emission dominates ($10^5 < T < 4 \times 10^7 \text{K}$). Such a trend in the decline in luminosity is seen in various other Type II SNe, including SN 1993J in M81 and SN1999em in NGC 1637 (Immler & Lewin 2003). However, our measured temperature of the plasma is around 4 keV, which corresponds to the former range, which indicates that the decline of L_X is unusually steep in this case. It is likely that the poor resolution of the ASCA and ROSAT satellites might not have been able to fully eliminate point source contamination, thus overestimating the fluxes of the data.

6 CONCLUSIONS

In this paper, we have presented a GTO *XMM-Newton* observation of NGC 891, a nearby edge-on spiral galaxy. We find that the diffuse X-ray emission protrudes from the disk in the NW direction out to approximately 6 kpc. The ex-

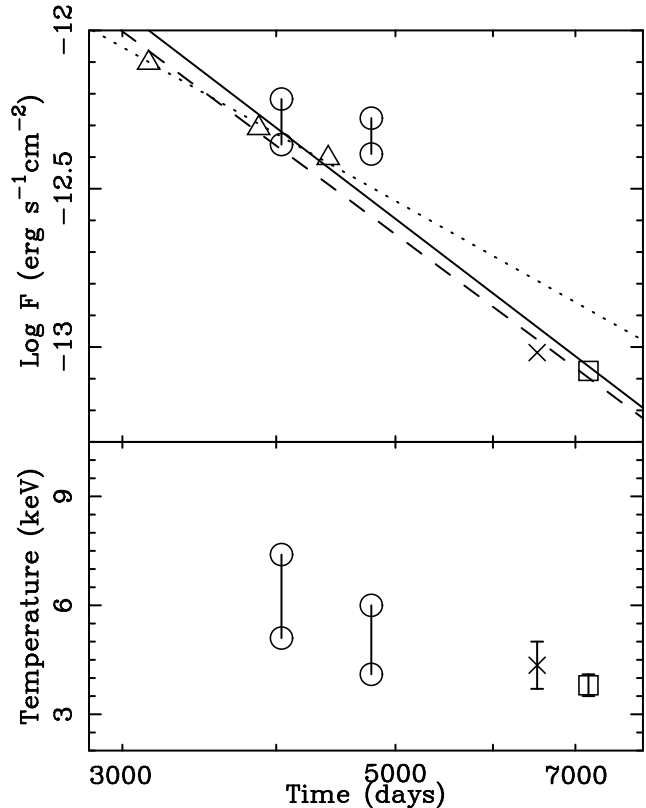


Figure 8. The X-ray lightcurve of SN1986J. ROSAT data are shown by triangles; ASCA data by circles; Chandra data denoted by a cross; and XMM-Newton by a square. The ASCA data has been adjusted to remove point source contributions (see text). The lower values represent the point source corrected results. The x-axis represents the time in days since the supernova went off ($t = 0$, which is taken to be 1983.0). All data is in the soft energy range 0.5–2.5 keV. The solid line is the best fit line for all the data with adjusted ASCA data points. The dashed line is the best fit for the data excluding all ASCA points. The dotted line is the best fit from Houck et al. (1998) for ROSAT only. Bottom panel: Temperature.

traplanar hot gas was previously observed in ROSAT observations, but the XMM observation seems to show a sharp cut-off to this gas, showing that this might be the extent to which the gas has reached. We also find that the best fitting thermal plasma model seems to require two temperatures of 0.08 and 0.3 keV respectively, though the fit of a single-temperature plasma of 0.26 keV isn't much worse. This contradicts previous findings based on ROSAT observations (Bregman & Pildis 1994; Read & Ponman 2003).

We use an archived Chandra observation to study the point source population within the D_{25} ellipse of the galaxy. We use a robust maximum likelihood method to determine the slope of the cumulative luminosity function $N(> S) = S^{-\alpha}$, and find that the slope is rather shallow, $\alpha = 0.77^{+0.13}_{-0.10}$. We have verified that this isn't predominantly due to extinction, by plotting the XLF for the energy range $> 2 \text{keV}$, without much change on slope.

Using a sample of other local galaxies, we have compared the X-ray and infrared properties of NGC 891 with those of nearby 'normal' and starburst spiral galaxies. We conclude that NGC 891 has more abundant star formation

than a normal spiral, but does not have as extreme properties as starburst galaxies like NGC 253 and NGC 4945, and that it is most likely a starburst galaxy in a quiescent state.

We examine an X-ray version of the “Schmidt Law”, which correlates the rate of star formation in a galaxy to the mass or density of its available gas. We show that the diffuse X-ray luminosity, an indicator of gas mass, of nearby spirals scales with their far infra-red luminosity, as indicator of dust mass and star formation rate, as $L_X \propto L_{FIR}^{0.87 \pm 0.07}$, except for extreme starbursts, and NGC 891 does not fall in the latter category.

We study the supernova SN1986J in NGC 891 in both *XMM-Newton* and *Chandra* observations, nearly twenty years after its explosion. It was studied in the X-ray using ROSAT and ASCA almost a decade ago. The flux and temperature calculated in those studies of low spatial resolution could have significant contamination from their point sources and the diffuse emission. A direct comparison shows that the temperature of the SN remnant at the time of observation was 5×10^7 K, which is less than it was a decade ago, but it also reveals that the X-ray luminosity has been declining with time ($L_X \propto t^{-3}$) far more steeply than expected.

ACKNOWLEDGEMENTS

Our thanks to Trevor Ponman and Andrew Read for sharing their XMM GTO data with us, and their advice. We thank Ben Maughan, Irini Sakellou and Ed Colbert for useful comments and help in data analysis, and Joel Bregman for a very interesting discussion. We also thank an anonymous referee for useful comments. This publication makes use of data products from the Two Micron All Sky Survey, which is a joint project of the University of Massachusetts and the Infrared Processing and Analysis Center/California Institute of Technology, funded by the National Aeronautics and Space Administration and the National Science Foundation.

REFERENCES

- Allen R.J., Baldwin J.E., Sancisi R., 1978, *A&A*, 62, 397
 Alton P.B., Bianchi S., Rand R.J., Xilouris E.M., Davies J.I., Trewheila M., 1998, *ApJ*, 507, L125
 Bendo G.J., Joseph R.D., Wells M., Gallais P., Haas M., Heras A., Klaas U., Laureijs R.J., Leech K., Lemke D., Metcalfe L., Rowan-Robinson M., Schultz B., Telesco C., 2002, *AJ*, 123, 3067
 Bottinelli L., Gougouenheim L., Paturel G., de Vaucouleurs G., 1985, *A&AS*, 59, 43
 Bottinelli L., Gougouenheim L., Paturel G., Teerikorpi P., 1986, *A&A*, 156, 157
 Bregman J.N., Pildis R.A., 1992, *ApJ*, 398, 107
 Bregman J.N., Pildis R.A., 1994, *ApJ*, 420, 570
 Bregman J. N., Houck J. C., Chevalier R. A., Roberts M. S., 2003, *ApJ*, 596, 323
 Chevalier, R. A. & Fransson, C. 1994, *ApJ*, 420, 268
 Chugai N.N., 1993, *ApJ*, 414, L101
 Ciardullo R., Jacoby G.H., Harris W.E., 1991, *ApJ*, 383, 487
 Cohen M., Wheaton W. A., Megeath S.T., 2003 *AJ*, 126, 1090
 Colbert E.J.M., Heckman T.M., Ptak A.F., Strickland D.K., 2004, *ApJ*, 602, 231
 Crawford D. F., Jauncey D. L., Murdoch H. S., 1970, *ApJ*, 162, 405
 Dahlem M., Dettmar R.-J., Hummel E., 1994, *A&A*, 290, 384
 David L.P., Jones C., Forman W., 1992, *ApJ*, 388, 82
 de Vaucouleurs G., 1975, *ApJS*, 29, 193
 de Vaucouleurs G., de Vaucouleurs A., Corwin H.G., Buta R.J., Paturel G., Fouque P., 1991, *RC3 Catalogue Volume I*
 Doane N.E., Sanders W.T., Wilcots E.M., Juda M., 2004 accepted *ApJ* (astro-ph/0409663)
 Fabbiano G., Zezas A., Murray S.S., 2001, *ApJ*, 554, 1035
 Ferrarese L., Holland C.F., Huchra J. et al., 2000, *ApJS*, 128, 431
 Fransson C., Lundqvist P., Chevalier R. A., 1996, *ApJ*, 461, 993
 Griffiths R.E., Padovani P., 1990, *ApJ*, 360, 483
 Harris J., Calzetti D., Gallagher J.S. III, Conselice C.J., Smith D.A., 2001, *AJ*, 122, 3046
 Hawk J. C., Savage B. D., 1997, *AJ*, 114, 2463
 Hartwell J. M., Stevens I.R., Strickland D.K., Heckman T.M., Summers L.K., 2004, *MNRAS*, 348, 406
 Houck J.C., Bregman J.N., Chevalier R.A., Tomisaka K., 1998, *ApJ*, 493, 431
 Immler S., Lewin W. H. G., 2003, *LNP*, 598, 91
 Irwin J.A., Sarazin C.L., Bregman J.N., 2002, *ApJ*, 570, 152
 Jarrett T.H., Chester T., Cutri R., Schneider S.E., Huchra J.P., 2003, *AJ*, 125, 525
 Karachentsev I.D., Makarov D.I., Sharina M.E., Dolphin A.E., Grebel E.K., Geisler D., Guhathakurta P., Hodge P.W., Karachentseva V.E., Sarajedini A., Seitzer P., 2003, *A&A*, 398, 479
 Karachentsev I.D., Grebel E.K., Sharina M.E., Dolphin A.E., Guhathakurta P., Hodge P.W., Karachentseva V.E., Sarajedini A., Seitzer P., 2003, *A&A*, 404, 93
 Kennicutt R.C., 1998, *ARA&A*, 36, 189
 Kennicutt R.C., Armus L., Bendo G., et al., 2003, *PASP*, 115, 928
 Kilgard R.E., Kaaret P., Krauss M.I., Prestwich A.H., Raley M.T., Zezas A., 2002, *ApJ*, 573, 138
 Lehnert M.D., Heckman T.M., 1996, *ApJ*, 462, 651
 Lehnert, M.D., Heckman, T.M., Weaver, K.A., 1999, *ApJ*, 523, 575
 Leonard D.C., Filippenko A.V., Li W., Matheson T., Kirshner R.P., Chornock R., Van Dyk S.D., Berlind P., Calkins M.L., Challis P.M., Garnavich P.M., Jha S., Mahdavi A., 2002, *AJ*, 124, 249
 Maíz-Apellániz J., Cieza L., MacKenty J.W., 2002, *AJ*, 123, 1307
 Moorwood A.F.M., van der Werf P.P., Kotilainen J.K., Marconi A., Oliva E., 1996, *A&A*, 308, 1
 Moshir M., 1990, *IRAS Faint Source Catalogue version 2.0*
 Murdoch H. S., Crawford D. F., Jauncey D. L., 1973, *ApJ*, 183, 1
 Pooley D., et al., 2002, *ApJ*, 572, 932
 Puche D., Carignan C., 1988, *AJ*, 95, 1025
 Press W.H., Teukolsky S.A., Vetterling W.T., Flannery

Table 6. Luminosity function and flux data for a sample of nearby galaxies.

Galaxy	Distance (Mpc)		LF slope		100 μm flux (Jy)		Source	S_{60}/S_{100}	$\log L_{FIR}$ (erg s ⁻¹)	$\log L_B$ (erg s ⁻¹)	$\log L_X$ (erg s ⁻¹)	Area (arcmin ²)		
(1)	(2)		(3)		(4)			(5)	(6)	(7)	(8)	(9)		
N253	3.94	n	0.81 ± 0.15		e	1770.0	l	ISO	0.67	43.70	42.80	39.08	y	595.68
N891	9.08		0.77 ^{+0.13} _{-0.10}			126.0	m	ISO	0.40	43.69	42.67	39.78	z	143.14
N1291	8.6	q	1.07 ± 0.15		e	10.1	d	IRAS	0.17	42.20	42.74	39.14	f	74.47
N1482	22.0	a	-			45.8	a	ISO	0.77	44.0	42.42	40.57	z	5.06
N3184	11.12	r	1.11 ± 0.22		e	29.0	c	IRAS	0.31	42.77	42.33	39.18	ab	42.24
N3628	7.91	s	0.82 ± 0.20 :		b	106.0	c	IRAS	0.49	43.56	42.50	39.74	z	172.03
N4214	2.94	o	0.76 ± 0.20		g	29.0	c	IRAS	0.62	41.98	40.89	38.53	g	59.52
N4244	4.49	p	0.46 ± 0.30 :		b	208.7	c	ISO	0.40	41.65	41.35	37.85	z	216.95
N4449	4.21	p	0.51 ± 0.20 :		i	73.0	h	IRAS	0.49	43.05	41.48	39.23	i	37.82
N4945	3.60	p	0.70 ± 0.20 :		b	1415.5	d	IRAS	0.42	44.40	42.45	39.53	z	93.65
N5253	3.14	t	0.54 ^{+0.21} _{-0.16}		k	29.4	j	IRAS	1.04	41.94	40.81	38.35	k	19.79
N6503	5.27	p	0.37 ± 0.30 :		b	28.9	c	ISO	0.35	42.38	41.66	38.85	z	20.47
M82	3.89	u	0.50 ± 0.08		e	1351.1	d	IRAS	0.94	44.27	42.45	40.63	z	98.87
M83	4.51	x	1.38 ± 0.28		e	638.6	d	IRAS	0.41	43.65	42.59	-		127.32
IC5332	4.63	v	1.30 ± 0.31		e	5.1	d	IRAS	0.16	41.87	40.97	-		39.98
Antennae	13.8	w	0.53 ± 0.07		e	82.0	c	IRAS	0.59	44.30	42.54	40.43	aa	22.05

NOTES.- Column (2): distance in Mpc, see text in §2 for distance discussion for NGC 891. Column (3): modulus of slope generated from the luminosity function. Data with a : has had the error estimated. Column (4): *ISO/IRAS* 100 μ m flux in Jansky. Column (5): Ratio of *IRAS/ISO* 60 to 100 μ m flux ratio. Column (6): Far IR luminosity calculated using Eqs 6 and 7. Column (7): K-band luminosity calculated using equation 8. Column (8): the X-ray luminosity ($\log L_X$) estimated in the 0.3–2.0 keV energy range. Column (9): Deprojected Galaxy area = πa^2 , where a is the semi-major axis of the D_{25} isophotal ellipse.

REFERENCES.-a) Kennicutt et al. (2003), b) Colbert et al. (2004), c) Soifer et al. (1989), d) Rice et al. (1988), e) Kilgard et al. (2002), f) Irwin, Sarazin & Bregman (2002), g) Hartwell et al. (2004), h) Thronson et al. (1987), i) Summers et al. (2003), j) Moshir et al. (1990), k) Summers et al. (2004), l) Radovic, Kahanpää & Lemke (2001), m) Alton et al. (1998), n) Karachentsev et al. (2003b), o) Maíz-Apellániz, Cieza & MacKenty (2002), p) Karachentsev et al. (2003a), q) de Vaucouleurs (1975), r) Leonard et al. (2002), s) Bottinelli et al. (1985), t) Ferrarese et al. (2000), u) Sakai & Madore. (1999), v) Bottinelli et al. (1986), w) Saviane, Hibbard & Rich (2004), x) Thim et al. (2003), y) Strickland et al. (2002), z) Strickland et al. (2004), aa) Fabbiano, Zezas & Murray (2001), ab) Doane et al. (2004).

B.P., 1986, Numerical Recipes in FORTRAN, 2nd Ed, Camb. Univ. Press, P660
 Radovic M., Kahanpää J., Lemke D., 2001, A&A, 377, 73
 Ranalli P., Comastri A., Setti G., 2003, A&A, 399, 39
 Read A.M., Ponman T.J., 2003, A & A, 409, 395
 Read A.M., Ponman T.J., Strickland D.K., 1997, MNRAS, 286, 626
 Rice W., Lonsdale C.J., Soifer B.T., Neugebauer G., Kopan E.L., Lloyd L.A., deJong T., Habing H.J., 1988, ApJS, 68, 91
 Rossa J., Dettmar R., Walterbos R. A. M., Norman C. A., 2004, AJ, 128, 674
 Rupen M.P., 1991, AJ, 102, 48
 Rupen M.P., van Gorkom J.H., Knapp G.R., Gunn J.E., Schneider D.P., 1987, AJ, 94, 61
 Sakai S., Madore B.F., 1999, ApJ, 526, 599
 Saviane I., Hibbard J.E., Rich R.M., 2004, AJ, 127, 660
 Shopbell, P. L., Bland-Hawthorn, J., 1998, ApJ, 493, 129
 Scoville N.Z., Thakkar D., Carlstrom J.E., Sargent A.I., 1993, ApJ, 404, L59
 Schmidt M., 1959, ApJ, 129, 243
 Sofue Y., Nakai N., 1993, PASJ, 45, 139
 Soifer B.T., Boemer L., Neugebauer G., Sanders D.B., 1987, AJ, 98, 1766
 Strickland C.K., Stevens I.R., 1999, MNRAS, 306, 43
 Strickland D.K., Ponman T.J., Stevens I R., 1997, A&A, 320, 378
 Strickland D.K., Heckman T.M., Weaver K.A., Dahlem M.,

2000, AJ, 120, 296
 Strickland D.K., Heckman T.M., Weaver K.A., Hoopes C.G., Dahlem M., 2002, ApJ, 568, 689
 Strickland D.K., Heckman T.M., Colbert E.J.M., Hoopes C.G., Weaver K.A., 2004, ApJSS, 151, 193
 Sukumar S., Allen R.J., 1991, ApJ, 382, 100
 Summers L.K., Stevens I.R., Strickland D.K., Heckman T., 2003, MNRAS, 342, 690
 Summers L.K., Stevens I.R., Strickland C.K., Heckman T., 2004, MNRAS, 351, 1
 Swaters R. A., Sancisi R., van der Hulst J. M., 1997, ApJ, 491, 140
 Terenio-Tagle G., Silich S., Muñoz-Tuñón, 2003, RevMexAA, 18, 136
 Thim F., Tammann G.A., Saha A., Dolphin A., Sandage A., Tolstoy E., Labhardt L., 2003, ApJ, 590, 256
 Thronson H.A., Hunter D.A., Telesco C.M., Decher R., Harper D.A., 1987, ApJ, 317, 180
 Tonry J.L., Dressler A., Blakeslee J.P., Ajhar E.A., Fletcher A.B., Luppino G.A., Metzger M.R., Moore C.B., 2001, ApJ, 546, 681
 van der Kruit P.C., 1984, A & A, 140, 470
 Valentijn E. A., van der Werf P. P., 1999, ApJ, 522, L29
 Wainscoat R.J., de Jong T., Wesselius P.R., 1987 A & A, 181, 225